CrossMark

ORIGINAL PAPER

Protective Aluminide Coatings for Refractory Metals

A. S. Ulrich[1] · M. C. Galetz[1]

Abstract Refractory metals are promising materials for high-temperature applications. However, these materials exhibit low oxidation resistance at elevated temperatures. To overcome this problem, aluminum diffusion layers were applied to molybdenum, niobium, tantalum, and tungsten using a pack cementation process. The coated samples were characterized using EPMA, optical microscope, and XRD. Homogeneous diffusion layers of different intermetallic phases were identified. The observed phases were in agreement with phase predictions made using thermodynamic calculations. Oxidation tests at 1300 °C for up to 100 h in synthetic air were carried out on uncoated as well as aluminized samples. The oxidation kinetics were analyzed via TGA measurements. After oxidation, the formed oxides and the remaining aluminum diffusion layers were characterized. It was found that an additional halogen treatment can significantly reduce oxidation attack of the substrate and support the formation of a continuous protective Al_2O_3 layer.

Keywords Intermetallics (aluminides) · Refractory metals · Pack cementation coatings · High-temperature applications · Oxidation resistance

Introduction

Recently, refractory metals and their alloys have received increasing attention for the purpose of substituting Ni-based single crystal superalloys. Refractory metals have significantly higher melting points compared to commonly used materials, while their mechanical properties are adequate at high temperatures [1, 2]. The main

✉ A. S. Ulrich
ulrich@dechema.de

M. C. Galetz
galetz@dechema.de

1   DECHEMA-Forschungsinstitut, Theodor-Heuss-Allee 25, 60486 Frankfurt am Main, Germany

challenges for their application are their low ductility at room temperature as well as low oxidation resistances at elevated temperatures. This study investigates an approach to enhance the oxidation resistance of the four different refractory metals tantalum, niobium, molybdenum, and tungsten. Considering the substrate materials, Nb_2O_5, Ta_2O_5, and WO_3 are fast growing oxides, whereas MoO_3 and WO_3 are even volatile. Aluminum diffusion layers manufactured by pack cementation are promising coatings used to suppress harmful oxidation by forming a dense and protective Al_2O_3 layer, thus preventing the underlying substrate from degenerative oxidation. Along with low fabrication costs, these coatings also show self-healing effects if the protective surface oxide layer fails.

Up to now, only a few pack cementation experiments have been done on refractory metals or their alloys. Most investigations were conducted on siliconizing of molybdenum-based alloys such as Mo–Si–B [3–6], Mo–W [7], and Mo-based TZM (titanium, zirconium, carbon) [8]. Pack aluminizing on Mo-Si-B alloys was shown to form a Mo_3Al_8-rich surface coating layer [9].

Initial investigations of pack-cemented coatings on pure refractory metals (niobium and tantalum) were done by Majumdar et al. [10, 11], using pack compositions of 7 wt% Al, 87 wt% Al_2O_3, 6 wt% NH_4F and 7 wt% Al, 7 wt% Si, 81 wt% Al_2O_3, 5 wt% NH_4F. Based on these experiments, a pack process time of 8 h was found to be sufficient to build smooth and homogeneous intermetallic phases.

Besides coating manufacturing, very little has been reported in the literature concerning oxidation resistance tests on aluminized refractory metals. Aluminum-silicide coatings on Mo-30W (10 wt%) alloys showed low mass gains (0.35 mg/cm^2) after oxidation in dry air for 10–15 h at 1100 °C [7]. Investigations of the oxidation resistance of aluminum diffusion coatings on niobium showed the formation of a 5–7-μm-thick protective Al_2O_3 layer after oxidation for 10 h at 1000 °C in dry air [10]. Good oxidation resistance with marginal weight gain was also observed with aluminum-silicide coatings on niobium and tantalum during oxidation tests at 1300 °C in dry air for up to 10 h [11]. It is remarkable that no studies beyond 15 h oxidation time could be found.

The protective effect of alumina-forming alloys or intermetallic phases on coating systems can be further improved by the so-called positive halogen effect [12]. The halogen effect was shown to improve protective oxide scale formation during high-temperature oxidation as often demonstrated for TiAl. The treatment promotes the aluminum oxidation while simultaneously reducing the oxidation of titanium. The formation of a smooth, homogeneous, and closed Al_2O_3 scale is supported and the possibility of destruction through fast growing metal oxides is reduced. The closed Al_2O_3 layer then serves as a diffusion barrier for oxygen, hence the underlying material is protected. In order to achieve the halogen effect, an additional surface treatment with halogens is needed before exposure to oxygen at high temperatures. One way to deposit halogens on the surface is spraying the sample surface with a halogen-containing polymer. All halogens are able to generate this effect but fluorine was found to be the most effective at least on TiAl [13]. In this study, fluorine treatment was applied to aluminized refractory metals for the first time. Because of its easy handling, the fluorocarbon polymer

polytetrafluoroethylene (PTFE) treatment was chosen. Its advantageous effect on oxidation resistance was investigated up to 100 h.

In summary, there has been some research on the aluminization of high-temperature refractory metals and their alloys via pack cementation processes reported in literature. However, a direct comparison of aluminum diffusion layers formed on different refractory metals under the same pack cementation conditions and their effect on oxidation resistance is currently lacking. This work will make an initial attempt to compare aluminide coatings on different refractory metals systematically.

Experimental Procedures

The substrate materials used in this work are four different kinds of refractory metals—molybdenum, niobium, tantalum, and tungsten. The substrates were produced and supplied by PLANSEE with a purity of >99.97 wt% for molybdenum, 99 wt% for niobium, 99.95 wt% for tantalum, and >99.97 wt% for tungsten. The samples were cut to 10 mm × 10 mm × 3 mm using wire erosion and cleaned for 10 min in acetone in an ultrasonic bath.

The refractory metal samples were embedded in the powder pack in a covered alumina crucible with an amount of powder-to-surface area ratio of 7.9 g/cm^2. A pack composition of 1 wt% Al, 1 wt% NH_4Cl, and 98 wt% Al_2O_3 was chosen according to experiments on austenitic steels [14]. This composition has a slightly higher donor-to-activator ratio than the pack powders used by Majumdar et al. [10, 11]. The resulting higher pack activity should ensure sufficient flux of aluminum atoms into the samples.

The crucible was placed in the middle of a tube furnace equipped with a quartz tube. The heat treatment of the crucible takes place at 1000 °C for 8 h under an Ar—5 % H_2 atmosphere with a constant flow rate of approximately 4 L/h. After the pack cementation process was completed, the coated specimens were cleaned with a brush and distilled water.

Following the coating procedure, the protective properties of the formed interdiffusion layers were tested using thermogravimetry (TGA). The mass change of the sample per unit surface area was measured during oxidation at 1300 °C in dry air up to 100 h. Samples without any diffusion coating were also oxidized to demonstrate the influence of the protective oxide layer formation. The samples were put into a cage made out of platinum wire covered by small aluminum oxide tubes, which was connected to the balance by an alumina bar. The furnace was heated at a rate of 20 °C/min to 1300 °C. When the target temperature was achieved, the atmosphere was changed to dry air (20.5 % O_2, 79.5 % N_2 with a flow rate of 4 × 10^{-4}m/s). Experiments were carried out for up to 100 h. After the exposure, the furnace was turned off and cooled down in dry air.

In order to further improve the protective nature of the aluminized samples, the use of a halogen treatment was investigated. Following the pack cementation process, the sample surface was sprayed with PTFE as described in [15] for titanium

aluminide alloys. After fluoration, the samples were dried and oxidized as described above.

The surface of all substrate materials was investigated before and after pack cementation process and after oxidation using X-ray diffraction measurements (XRD). The samples were nickel-plated and a cross section of each sample was mounted in epoxy resin, ground with successively finer silicon carbide papers from 500 to 1000 grit, polished with 3 and 1 μm diamond suspensions, and subsequently relief polished. The investigation of the microstructure of the coatings as well as the measurement of the interdiffusion layer thickness was done using optical microscopy. Additionally, element mapping and concentration profile measurements were carried out using electron probe microanalysis (EPMA). The intermetallic phases and their composition were identified by combining EPMA measurements and XRD patterns.

Aluminum Diffusion Coatings

Intermetallic Phase Predictions by Investigation of Aluminum Activities

Using a theoretical approach [16], predictions of the formed intermetallic phases during the pack cementation process were made in advance. First, the pack parameters were optimized to form suitable interdiffusion layers containing a high aluminum reservoir. Later, the predictions were compared to the experimental results.

In order to predict the phases formed after the pack cementation process using the chosen pack parameters (8 h at 1000 °C, 7.9 g/cm^2, 1 wt% Al, 1 wt% NH$_4$Cl, 98 wt% Al$_2$O$_3$) comparable experiments in the literature and thermodynamic calculations using the program FactSage 6.1 (databases ELEM, 8099, 9277, 9271, 9275, 9109, and MoAl) [17] were taken into account.

Whether a coating with a high or a low aluminum content formed depended on the aluminum activity in the pack and on the aluminum flux into the sample material. This flux is determined by the activity difference between the pack and the substrate which has to be positive to provide an aluminum flux into the sample. This activity in the pack powder also determines the activity at the surface and thus the intermetallic phase formed at the gas–metal interface. Therefore, higher pack activities lead to the formation of intermetallic phases with higher aluminum contents [18]. The phase evolution below the surface is then controlled by the interdiffusion and phase transformation behavior of the "diffusion couple".

The aluminum activity of the pack can be determined by the sum of the partial pressures of the relevant aluminum releasing chlorides AlCl, AlCl$_2$, and AlCl$_3$ (see Fig. 1). Other chlorides like Al$_2$Cl$_6$ or AlCl$_2$H are also predicted by thermodynamic calculations, but they have either negligible partial pressures at the relevant temperature or release a negligible amount of aluminum and therefore are not considered relevant for the aluminum activity in the pack. In total, the calculated partial pressure and activity of relevant chlorides for a pack composition of 1 wt%
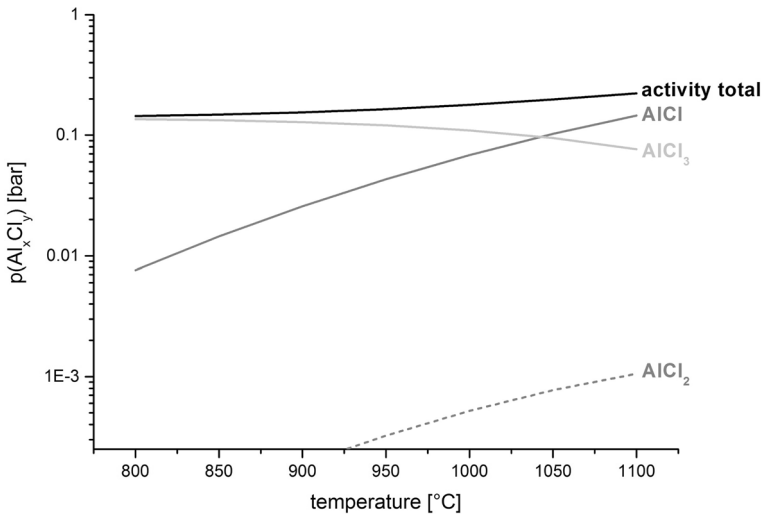
Fig. 1 Partial pressures of relevant aluminum carrying chlorides and their total partial pressure over pack process temperature. The total pressure also determines the aluminum activity of the pack powder

Al, 1 wt% NH_4Cl, and 98 wt% Al_2O_3 is 0.18 at the process temperature of 1000 °C as shown by the black curve in Fig. 1.

The activities of aluminum in the binary Mo–Al phase diagram and thus at the different phase boundaries can also be calculated via FactSage 6.1. The result of the calculation is shown in Fig. 2. The aluminum activities calculated over the stability range of the Al_4Mo, the Al_8Mo_3, and the $AlMo_3$ phases are compared to the pack activity given in Table 1.

Due to the fact that the activity difference between the pack powder and the intermetallic phase at the substrate's surface must be positive, an intermetallic phase with a lower activity than in the pack but still with the highest possible aluminum content is formed at the surface. Thus, as exemplified for the Mo–Al system, an Al_8Mo_3 layer is expected to form because its minimum activity (0.08 at 1000 °C) is lower than the pack activity (0.18 at 1000 °C). It should be mentioned that not only the aluminum activity of the pack can determine the formed intermetallic phases but also the diffusion rate in the formed intermetallic layer. Apart from the activity difference between the intermetallic phase and the gas phase, there is also an activity gradient between the intermetallic phase and the bulk material. This activity gradient further drives aluminum diffusion from the intermetallic phase into the bulk material, thickening the coating over time. Since no further refractory metal–aluminum systems are available in the FactSage databases, the intermetallic phase prediction is exemplified only for the aluminizing of molybdenum.

Concerning niobium, the phase with the highest aluminum content in the binary Nb–Al phase diagram—Al_3Nb—is expected to form during pack cementation according to the aluminizing experiments done by Majumdar et al. [10]. In these experiments, an even lower aluminum/activator mass ratio was used which is equal to a lower aluminum activity of the pack powder, thus Al_3Nb is expected in the
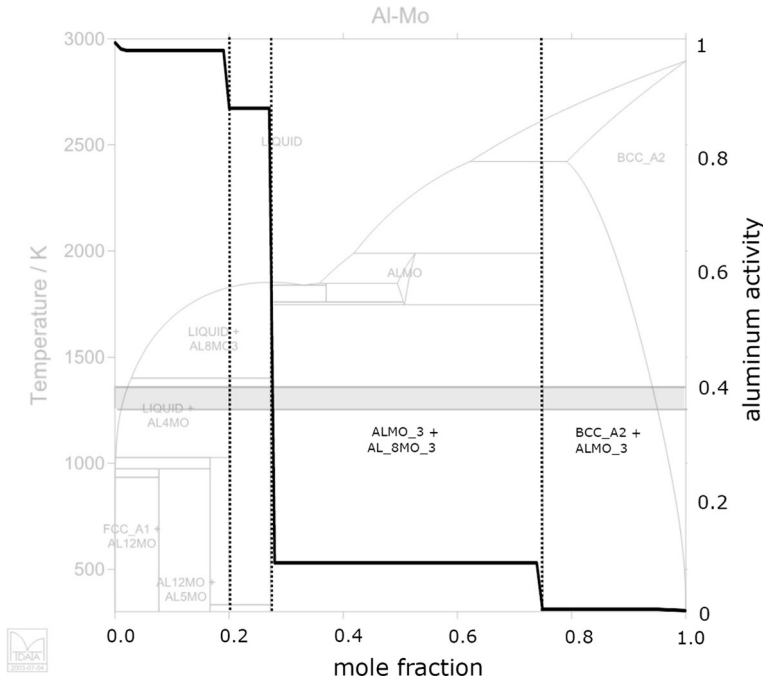
Fig. 2 Aluminum activity curve at 1000 °C over the different phases in a binary Al–Mo phase diagram after [30]

Table 1 Aluminum activity in the pack powder in comparison to the aluminum activity ranges in relevant intermetallic phases of the Al–Mo phase diagram calculated for the process temperature of 1000 °C

Temperature	Pack powder	Al$_4$Mo	Al$_8$Mo$_3$	AlMo$_3$
1000 °C	0.18	0.89–0.99	0.08–0.89	0.003–0.08

current experiments as well. In the case of aluminizing of tantalum and tungsten, no comparable experiments exist in the literature. However, due to the fact that in tungsten only a single Al$_4$W intermetallic phase exists at the temperature of 1000 °C this phase is expected to form. For tantalum, the situation is more complex because besides Al$_3$Ta, which is the intermetallic phase with the highest aluminum content, four other phases exist in this temperature range.

To sum up, the intermetallic phases Al$_3$Nb on niobium, Al$_8$Mo$_3$ on molybdenum, and Al$_4$W on tungsten are expected to form during experiments at a process temperature of 1000 °C using pack compositions in the range of 1 wt% Al, 1 wt% NH$_4$Cl, and 98 wt% Al$_2$O$_3$. Following the predictions made above for molybdenum and the other refractory metals, the experimental results are shown in the following and are compared to the predictions.

### Results of the Pack Aluminizing Experiments

The phases found in niobium, tantalum, tungsten, and molybdenum after pack aluminizing were identified via EPMA and XRD measurements. The analysis is schematically exemplified for niobium in Fig. 3. Using EPMA, the concentration ratio of aluminum and niobium corresponding to the Al_3Nb phase is identified and confirmed by XRD measurement. Besides Al_3Nb, some oxygen and nitrogen impurities were also found. These impurities are not desirable; however, they are not critical for the coating performance because the overall percentage in the diffusion layer is low and higher percentages are only observed as oxides on the substrate surface which indicates post-process formation.

Figure 4 shows optical micrographs of the aluminide coatings formed after a pack process for 8 h at 1000 °C. On niobium, an Al_3Nb layer and on tungsten an Al_4W layer were formed, while on the tantalum substrate an Al_3Ta diffusion layer was found. On the molybdenum substrate a duplex layer is formed, consisting of a 34 ± 1-µm-thick Al_8Mo_3 layer and an inner $AlMo_3$ sublayer with a thickness of 4.6 ± 0.2 µm at the Al_8Mo_3/molybdenum interface.

Similar to NiAl-grains formed on NiAl-alloys after aluminizing above 1000 °C [19], the grains in the refractory metal intermetallic phases have a columnar grain structure (see Fig. 4). The grains are also elongated over the whole intermetallic layer. The elongation develops in the diffusion direction, and therefore the shape and orientation of the grains reflect the direction of the coating growth. Along the grain boundaries of the intermetallic phases, some intergranular cracks have evolved in all coated samples; however, this crack formation is more pronounced in the Al_3Nb and Al_3Ta phases. In contrast to the other refractory metal aluminides, not only intergranular but also intragranular cracks evolved in Al_3Nb.
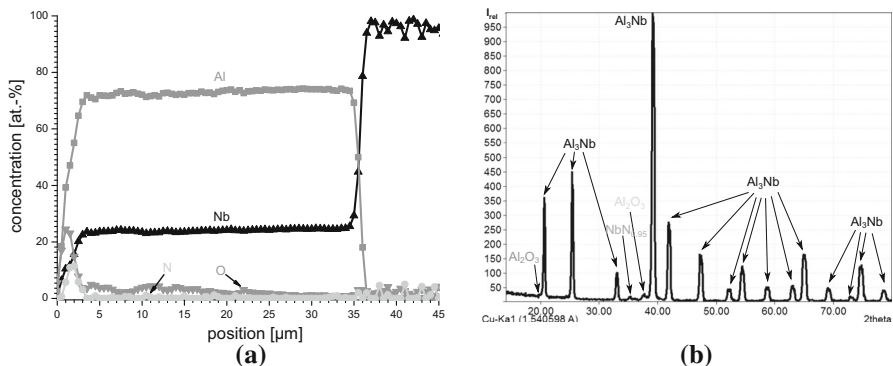
Fig. 3 Analysis of intermetallic phase formed on niobium after pack aluminizing for 8 h at 1000 °C. **a** EPMA line scan showing the concentration profiles of niobium and aluminum for phase identification and the impurities of oxygen and nitrogen. The Al_3Nb phase is found due to a Al:Nb concentration ratio of 3 (aluminum 72.9 at.% and niobium 24.8 at.%). **b** XRD measurement of the sample confirming the formation of the Al_3Nb phase
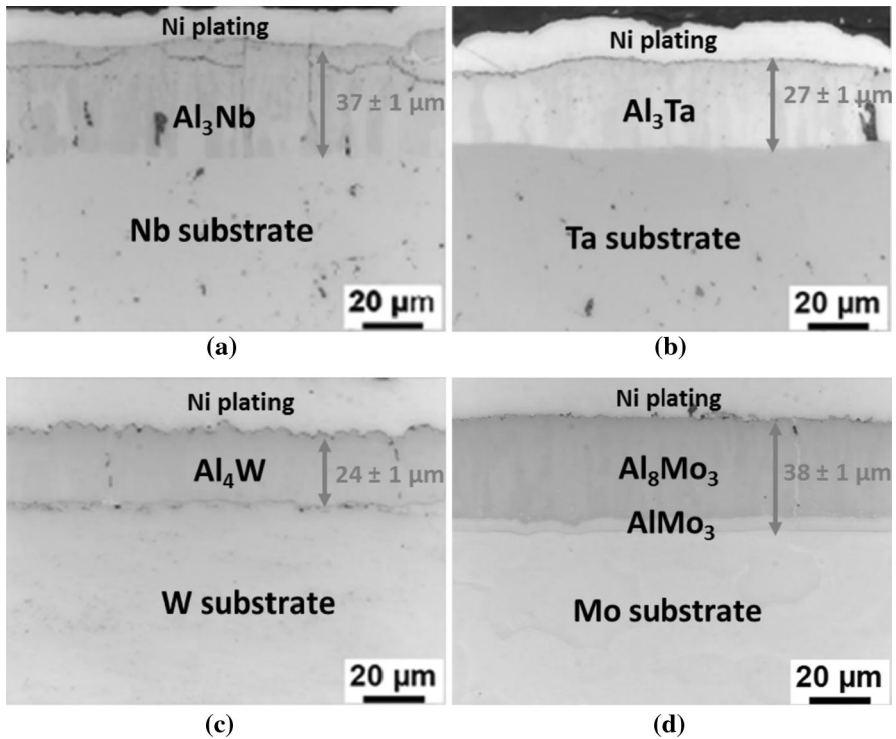
Fig. 4 Optical micrograph of the **a** niobium substrate, **b** tantalum substrate, **c** tungsten substrate, and **d** molybdenum substrate after pack cementation with aluminum at 1000 °C. The intermetallic Re_xAl_y layers and their thicknesses (*arrows*) are marked. The white layer on top of all substrates consists of nickel. This layer is deposited after the pack cementation process to improve the contrast of the intermetallic layers in the pictures and EPMA measurements and therefore it is not relevant for the experimental results

Comparison of Phase Predictions and Experimental Results

On the molybdenum substrate Al_8Mo_3 is found as was predicted by the thermodynamic calculations of the aluminum activities. In addition, a thin intermetallic sublayer is found at the Al_8Mo_3/molybdenum interface which was identified as $AlMo_3$. The $AlMo_3$ phase has a lower aluminum content and therefore its appearance is a sign of interdiffusion between the Al_8Mo_3 layer and the substrate. Interdiffusion occurs if the aluminum supply at the Al_8Mo_3/molybdenum interface is insufficient to sustain further Al_8Mo_3 growth. This happens if the aluminum activity in the pack drops below the activity of the primarily formed intermetallic phase (Al_8Mo_3) or if transport of aluminum through the Al_8Mo_3 layer is lowered as the Al_8Mo_3 layer grows and does not provide a sufficient aluminum flux at the coating/substrate interface after a certain process time. In both cases, the aluminum flux to the Al_8Mo_3/molybdenum interface decreases. However, there is still an aluminum activity difference at the Al_8Mo_3/molybdenum interface which drives aluminum diffusion from the Al_8Mo_3 layer into the substrate and

molybdenum counterdiffusion from the bulk material. The resultant intermetallic phase with a lower aluminum content than Al_8Mo_3 at 1000 °C—the $AlMo_3$ phase—forms at the Al_8Mo_3/substrate interface. It should be noted that after 8 h at 1000 °C only the onset of the reactive aluminum depletion was observed. Thus its effect on the predictions—which are only valid under equilibrium conditions—can be neglected.

Further Al_3Nb phases formed on niobium confirmed comparable experiments reported in the literature [10]. On tungsten Al_4W was identified, and on tantalum the phase with the highest aluminum content was formed, which confirms again the high aluminum pack activity in line with the other aluminum-rich aluminides.

## Oxidation Tests

Results of the Oxidation Tests

All oxidation tests were carried out at 1300 °C in dry air. The weight changes per unit area were determined via TGA measurements. At first, the results of 12 h oxidation tests are shown followed by experiments for 40 and 100 h. In these experiments, uncoated and coated samples as well as coated samples with additional fluorine treatment were used.

Oxidation Tests for 12 h

The mass change curves of the 12 h oxidation tests are shown in Fig. 5. The broken lines show the mass change of uncoated substrates, the gray-dotted lines refer to the oxidation of aluminized substrates using the pack cementation process described above. The solid lines are the measured weight change curves of aluminized and additionally fluorine-treated samples.

In theory, a slow parabolic mass gain characteristic is a sign of protective oxide formation, while linear mass gain and mass loss are always signs of protection failure. All uncoated substrate materials show either catastrophic linear mass gain or mass loss characteristics. After 12 h of oxidation, the sample materials are either fully oxidized, which is the case for niobium, tantalum, and tungsten, or the substrate evaporates due to the formation of volatile oxides, which is the case for molybdenum. It must be mentioned that the TGA measurement shown for the uncoated and some aluminized substrates stop after a certain time when the measurement limit of the microbalance is reached. However, the oxidation continues until the substrate material is fully oxidized.

From Fig. 5a and c, it is obvious that the effect of pack aluminizing on the oxidation kinetics seems to be negligible in the case of tantalum and tungsten. With molybdenum and niobium, a slowing down of the oxidation kinetics is found. However, aluminized niobium is again fully oxidized after 12 h, whereas with aluminized molybdenum no mass loss is observed but a mass increase of 1.02 mg/cm^2 after 12 h. Cross-section analysis of aluminized molybdenum shows the formation of a
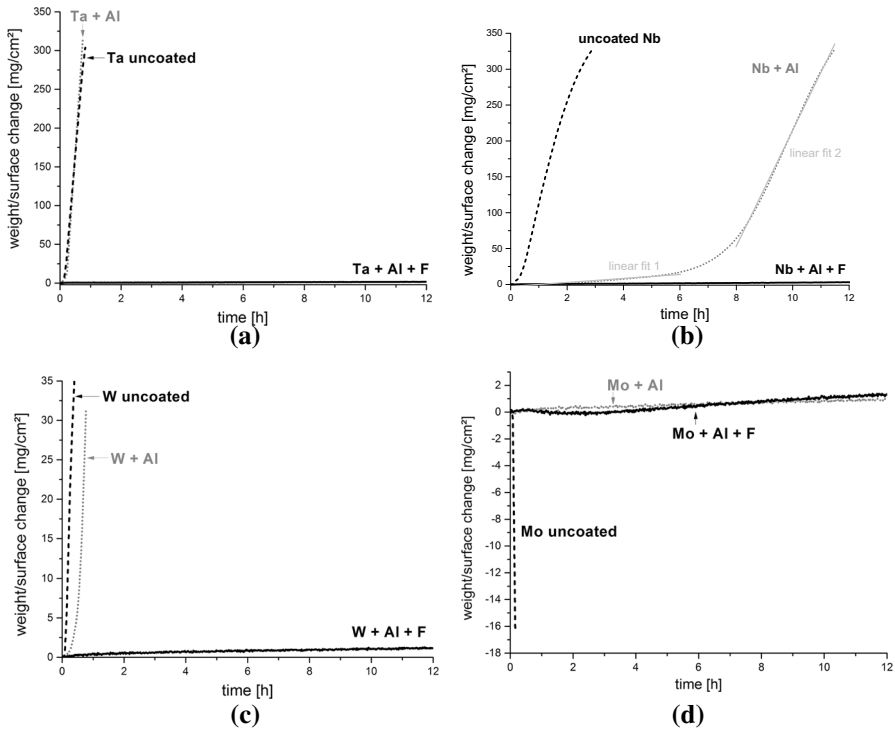
Fig. 5 Mass change curves from 12 h experiments carried out at 1300 °C in synthetic air: Characteristics of **a** tantalum substrates, **b** niobium substrates, **c** tungsten substrates, and **d** molybdenum substrates (note the different axes). For each substrate material, the kinetics of an uncoated sample, an aluminized sample, and an aluminized and additionally fluorine-treated sample are shown. In addition to the TGA curves on niobium, linear fits are added to (**b**) to analyze the growth rate in two regions

protective Al_2O_3 layer with a thickness of 5.8 ± 0.4 μm, while intermetallic phases still remain below the oxide layer providing an aluminum reservoir (see Fig. 7c).

An additional fluorine treatment after the aluminizing step shows a more promising effect on oxidation protection. A magnification of the oxidation curves of all fluorine-treated samples is shown in Fig. 6. The TGA experiments show that the oxidation rates of all fluorine-treated refractory metal samples are much lower than of the untreated samples and only small weight gains are observed after oxidation. Hence, similar to TiAl alloys, the fluorine treatment enhances the oxidation protection of refractory metals. Corresponding micrographs of the samples after oxidation tests are shown in Figs. 7 and 8. Similar to the aluminizing experiments, the phases were again analyzed using EPMA and XRD and marked in the micrographs. On tantalum and molybdenum thin closed Al_2O_3 layers are found, while on niobium and tungsten the substrate material is locally oxidized. The thicknesses of oxide and intermetallic phase layers are summarized in Table 2. Looking at the EPMA line scans (Figs. 7b, 8b, d, f), no fluorine is detected in molybdenum, niobium, and tungsten after oxidation, but low concentrations (1–3.5 at.% fluorine) are detected in tantalum. Comparing the aluminized molybdenum
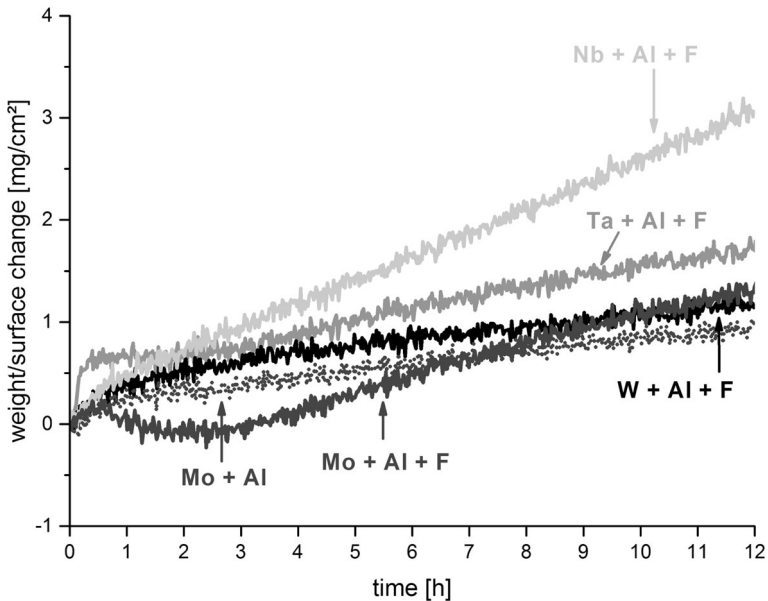
Fig. 6 Magnification of the mass change curves of aluminized and fluorine-treated refractory metal samples. Additionally, the characteristics of the aluminized molybdenum substrate without a fluorine treatment are shown. The measurement was done via TGA at 1300 °C in synthetic air

samples with and without fluorine treatment, no significant difference in layer structure and element concentration is found after oxidation. For niobium, additional EPMA element maps of niobium, oxygen, and aluminum are shown in Fig. 9. The measurements were carried out considering an area where no local oxidation had taken place yet. It becomes obvious that the aluminum reservoir near the Al_2O_3 layer is depleted in aluminum and a small, around 1–1.5-µm-thick Nb_2Al layer is formed in between the Al_2O_3 scale and $NbAl_3$.

Oxidation Tests for 40 h

Further oxidation tests at 1300 °C in synthetic air were carried out for 40 h varying the PTFE coverage ratio on pack-aluminized tantalum substrates. The substrates were again pack aluminized as described earlier. Afterwards, both samples were sprayed with PTFE; however, one was sprayed with twice the amount as was used in 12 h oxidation experiments and as it is commonly used on TiAl alloys [15]. In Fig. 10, the images of these samples after 40 h oxidation are shown. The sample which was treated with a single PTFE application is fully oxidized (Fig. 10a), while the sample treated with a double coverage of PTFE exhibits a closed Al_2O_3 layer with a remaining aluminum reservoir below (Fig. 10b). This demonstrates that the protective effect of the aluminum diffusion coatings depends highly on the amount of fluorine treatment. Similar to TiAl alloys a certain window of surface coverage
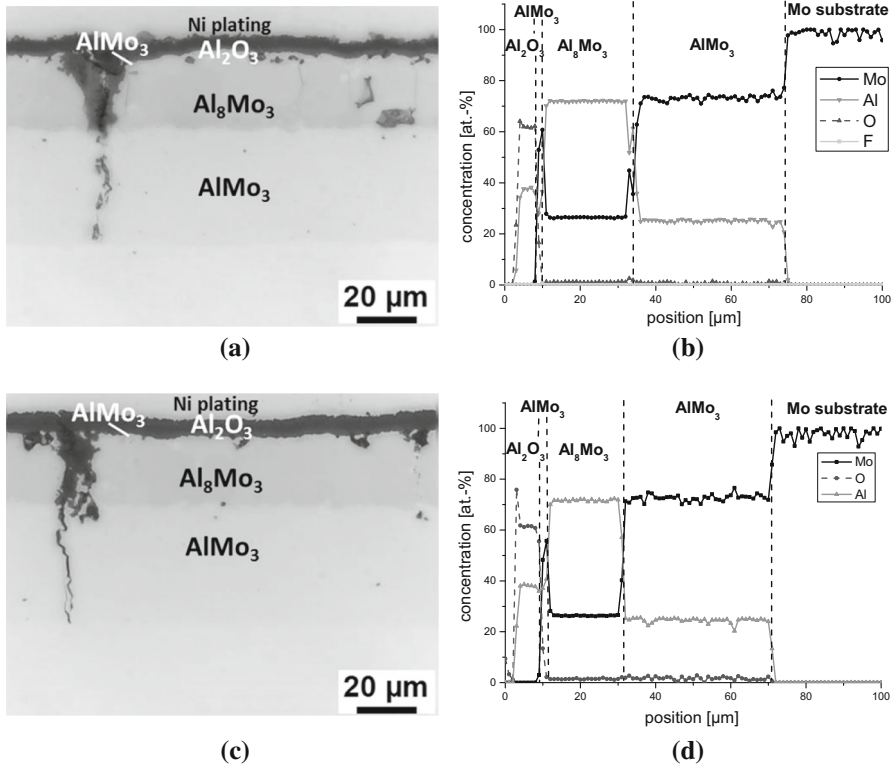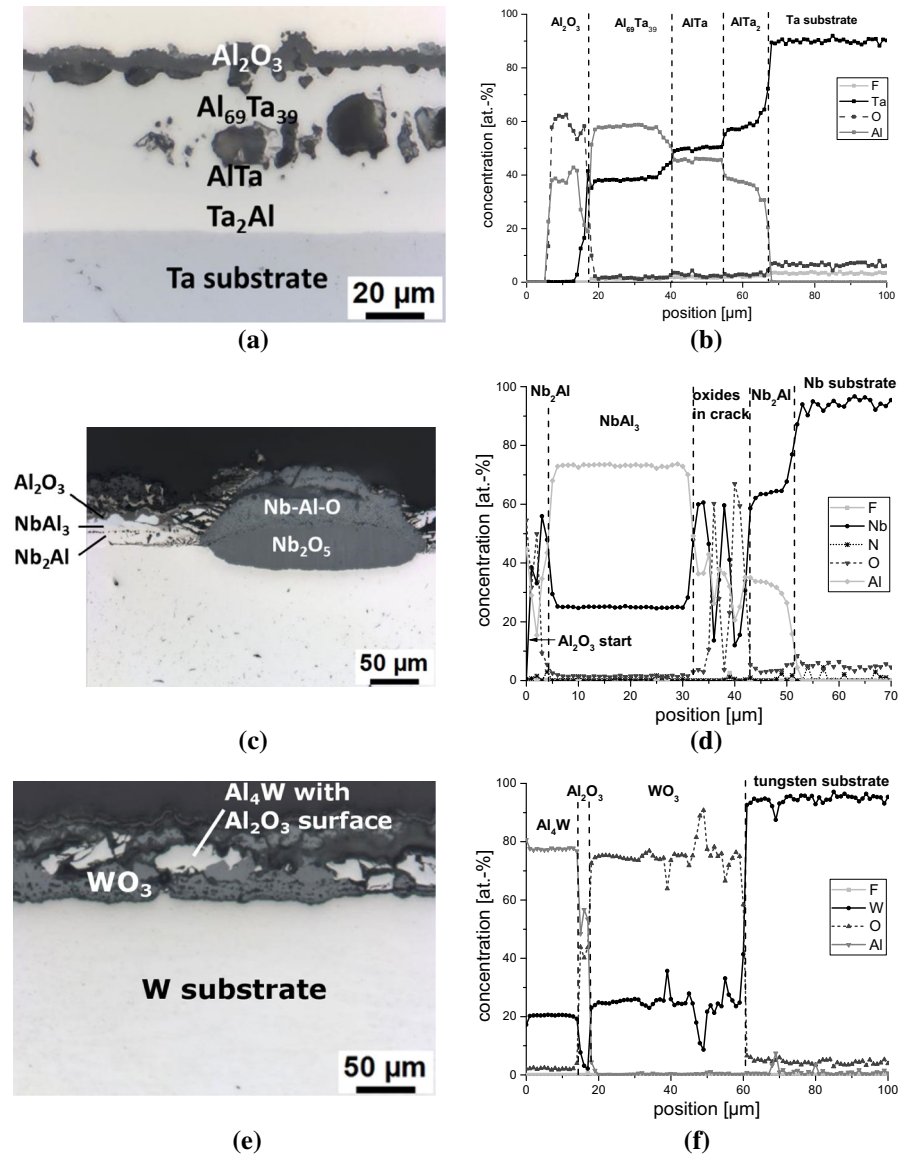
Fig. 7 Cross sections and concentration profiles of the aluminized molybdenum samples with and without fluorine treatment after oxidation tests for 12 h at 1300 °C. The concentration profiles are measured via EPMA perpendicular to the surface beginning at the oxide scale. **a** Micrograph and **b** EPMA line scan of fluorine-treated molybdenum sample. **c** Micrograph and **d** EPMA line scan of the samples not treated with fluorine. The identified oxides and intermetallic phases are marked in the cross sections. It becomes obvious that both molybdenum samples show good oxidation resistance due to the formation of a dense, homogeneous, and protective Al_2O_3 scale

range is expected for tantalum in which the fluorine treatment supports the Al_2O_3 scale formation [20].

Oxidation Tests of Samples with Optimized Surface Treatment for 100 h

The TGA measurements for 100 h are shown in Fig. 11. The scatter in the TGA curves occurs mainly due to inductive effects on the platinum containing cage during operation of the furnace. They seem to be more pronounced in the long-term experiments due to lower total mass gains; however, in all experiments they are in the same range. All samples were aluminized by pack cementation process as described earlier. As shown in the oxidation experiments for 12 h, fluorine treatment has no visible effect on aluminized molybdenum, therefore in the 100 h experiments molybdenum was not sprayed with PTFE. Niobium and tungsten were halogen treated the same way as for the 12 h experiments, but tantalum was coated with twice the

Fig. 8 Concentration profiles measured using EPMA and cross sections of aluminized and fluorine-treated tantalum, tungsten, and niobium samples after oxidation tests for 12 h at 1300 °C and the identified oxides and intermetallic phases are, again, marked in the cross sections: Micrograph (**a**) and EPMA line scan (**b**) of the fluorine-treated tantalum substrate. Micrograph (**c**) and EPMA line scan (**d**) of fluorine-treated niobium substrate. Micrograph (**e**) and EPMA line scan (**f**) of fluorine-treated tungsten substrate. The tantalum sample was found to show good oxidation resistance due to the formation of a dense, homogeneous, and protective Al_2O_3 scale, while on niobium and tungsten the underlying substrate material is oxidized and the layers tend to spall

Table 2 Measured oxide layer thicknesses and total diffusion layer thicknesses of the samples whose micrographs are shown in Figs. 7 and 8

	Mo + Al (μm)	Mo + Al + F (μm)	Ta + Al + F (μm)
Al_2O_3	5.8 ± 0.4	5.5 ± 0.3	6.4 ± 0.6
Coating zones after 12 h at 1300 °C	$AlMo_3$: 2.3 ± 0.4	$AlMo_3$: 1.8 ± 0.2	Al_3Ta_2: 9 ± 1
	Al_8Mo_3: 22 ± 1	Al_8Mo_3: 22 ± 1	AlTa: 33 ± 1
	$AlMo_3$: 38 ± 1	$AlMo_3$ 39 ± 1	Ta_2Al: 11 ± 1
		Nb + Al + F	W + Al + F
Al_2O_3		14 ± 4	–
Coating zones after 12 h at 1300 °C		Al_3Nb: 28 ± 3	$Al_2O_3 + Al_4W$:
		$AlNb_2$: 20 ± 1	65 ± 2
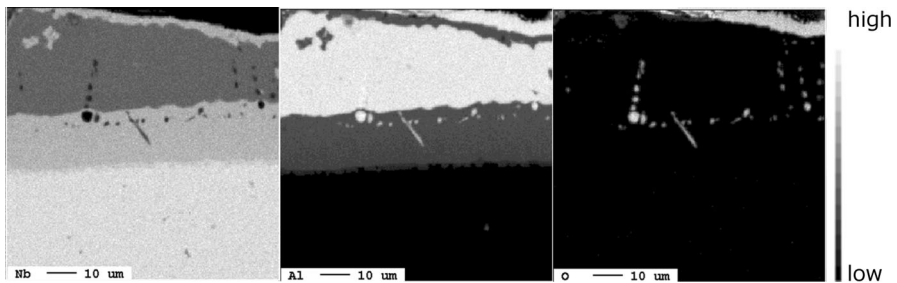
Fig. 9 EPMA element maps of Nb, Al, and O of an aluminized and fluorine-treated niobium substrate after 12 h of oxidation at 1300 °C in synthetic air. An area where no local oxidation has taken place yet is shown
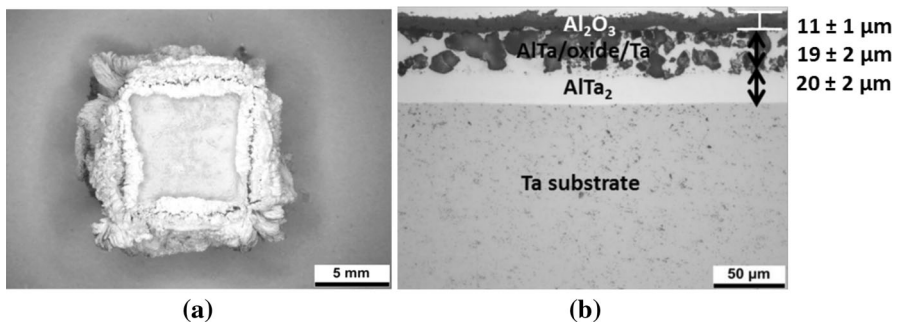
Fig. 10 Aluminized tantalum substrates with single (**a**) and double (**b**) fluorine treatment after oxidation at 1300 °C in synthetic air for 40 h

amount of PTFE with respect to the results gained in the 40-h oxidation experiments. The phases were again analyzed via EPMA and XRD measurements and marked in the cross sections. TGA measurements of tantalum and tungsten substrates show flat mass gain slopes with a total mass increase of around 0.94 mg/cm² of the tantalum substrate after 100 h of oxidation and with a total mass increase of around 0.77 mg/cm² of the
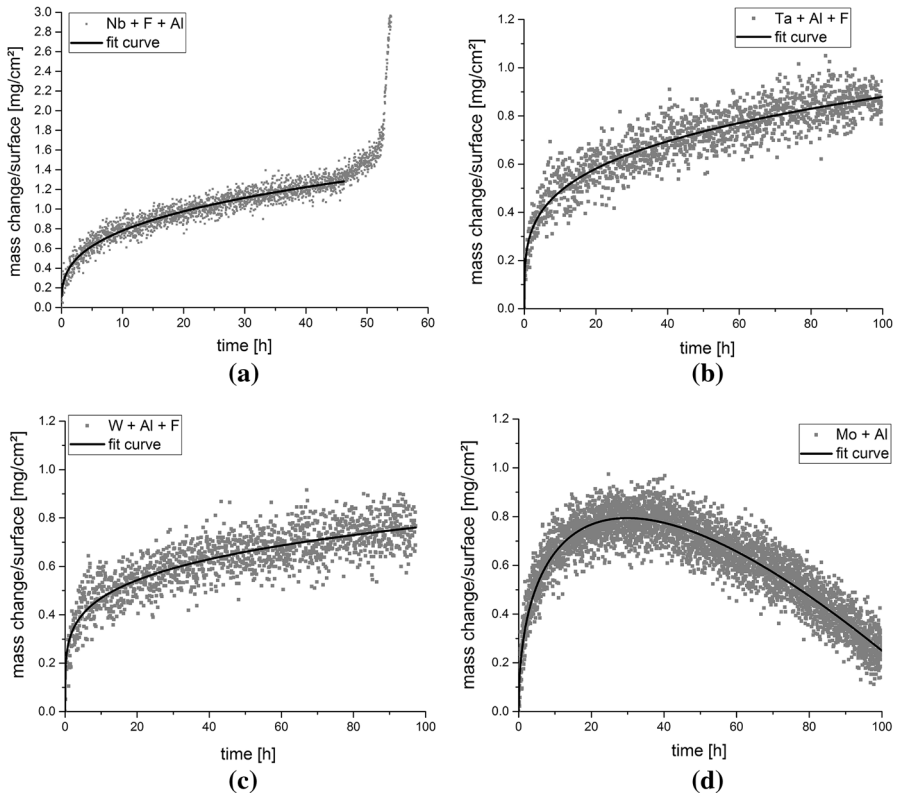
Fig. 11 TGA measurements of **a** aluminized and single fluorine-treated niobium substrate, **b** aluminized and double fluorine-treated tantalum substrate, **c** aluminized and single fluorine-treated tungsten substrate, and **d** aluminized molybdenum substrate. The experiments were carried out at 1300 °C in dry air. The mass change curves were fitted and the fits were added to the plots

tungsten substrate. While TGA measurements of tantalum and tungsten show parabolic behavior, niobium shows a fast mass gain after around 46 h and molybdenum a mass loss after around 30 h.

The corresponding cross sections of the substrates after 100 h of oxidation are shown in Fig. 12. The micrographs show that Nb_2O_5 had formed on niobium and neither an intermetallic phase nor Al_2O_3 was detected. On tungsten, localized oxidation occured and WO_3 is detected while locally the surface is still covered with the Al_4W phase. The aluminized and double fluorine-treated tantalum sample shows the formation of a closed and protective Al_2O_3 oxide scale and remanent intermetallic Ta–Al intermetallic phases below this scale. The EPMA line scan in Fig. 14 reveals a remaining fluorine content of 1.7–5 at.% in the substrate and in the intermetallic phases after oxidation. Also, on molybdenum an Al_2O_3 scale was found with an Al_8Mo_3 and $AlMo_3$ layer below. However, locally, the Al_8Mo_3 phase is fully consumed and an area with pores, Al_2O_3, metallic molybdenum (see BSE image in 13b), and an area consisting of aluminum, molybdenum as well as oxygen are detected. Looking at such an area with higher magnification (Fig. 13a), cracks in
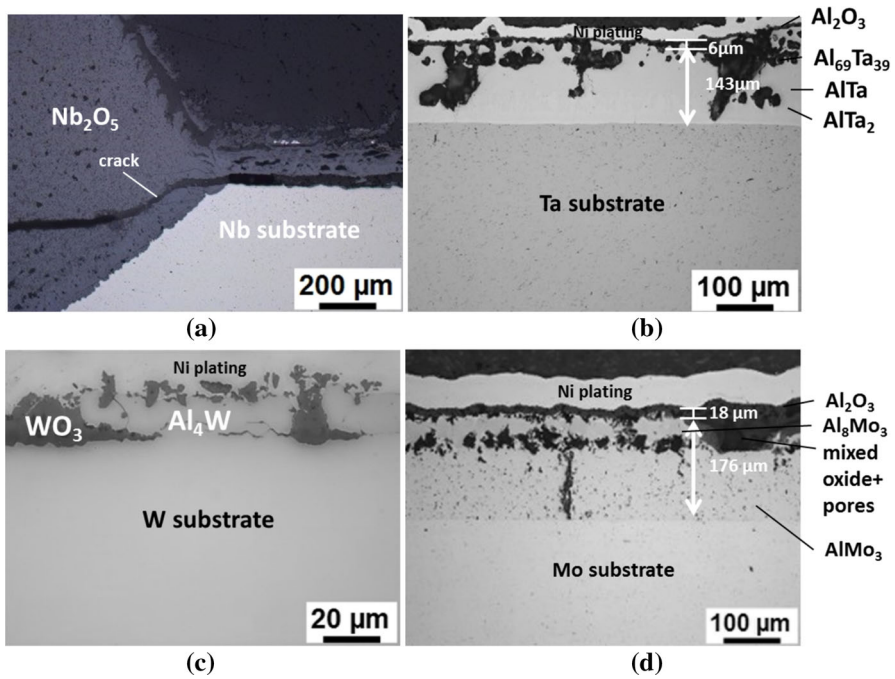
Fig. 12 Cross sections of **a** aluminized and single fluorine-treated niobium substrate, **b** aluminized and double fluorine-treated tantalum substrate, **c** aluminized and single fluorine-treated tungsten substrate, and **d** aluminized molybdenum substrate after 100 h of oxidation at 1300 °C in dry air
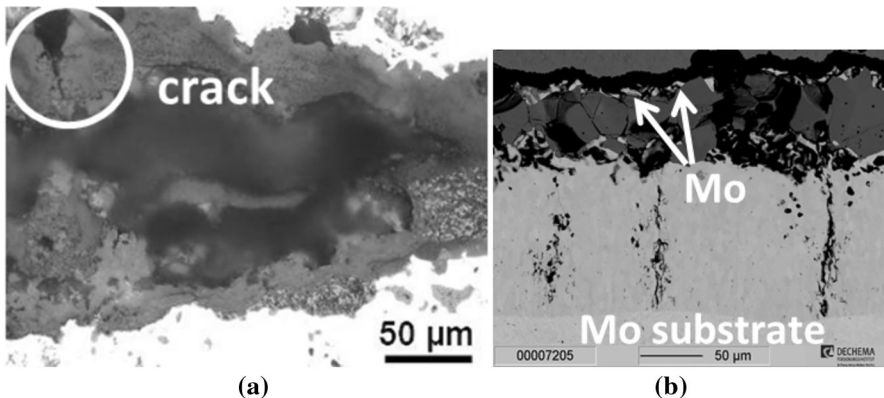
Fig. 13 In **a** a micrograph with a higher magnification of the molybdenum substrate than in Fig. 12d is shown and **b** is a BSE image of the same substrate

the Al_2O_3 layer are revealed. The layer thicknesses of the oxide layers and intermetallic phases of selected substrates are listed in Table 3. It is obvious that, compared to shorter oxidation tests and to the pack-aluminized samples, the total interdiffusion layer thicknesses have increased. Furthermore, on tantalum and molybdenum, Kirkendall porosity is found which is also a sign of fast diffusion.

Table 3 Measured oxide layer thicknesses and total interdiffusion layer thicknesses after oxidation at 1300 °C for 100 h. All samples were aluminized. Molybdenum is not fluorine-treated, while for tungsten a single and for tantalum a double fluorine treatment was used

	Mo + Al (μm)	Ta + Al + 2× F (μm)	W + Al + F (μm)
Al_2O_3	18 ± 4	5.9 ± 0.6	–
Coating zones after 100 h at 1300 °C	Al_8Mo_3 + Mo + $AlMo_3$ precipitates:	$Al_{69}Ta_{39}$: 92 ± 3	Al_4W + WO_3:
	52 ± 2	AlTa: 45 ± 2	17 ± 1
	$AlMo_3$: 124 ± 1	$AlTa_2$: 6.6 ± 0.2	

Analysis of Oxidation Processes

Oxidation of Tantalum

Oxidation of uncoated tantalum results in a linear mass gain characteristic due to fast growing and porous Ta_2O_5 (see Fig. 5a). During oxidation, numerous cracks evolve due to the high Pilling–Bedworth ratio (P-B ratio) and spallation takes place (see Table 5). Pack aluminizing shows no effect on tantalum although there is a high aluminum concentration at the surface (see Fig. 4b). Looking at the beginning of the oxidation process in more detail reveals that all elements which are present at the surface—in this case tantalum and aluminum—are oxidized. The formation of Al_2O_3 is in competition with the formation of the refractory metal oxide. Formation of a continuous Al_2O_3 scale highly depends on the local aluminum activity, on the formation rate of oxides, their P–B ratio, lattice mismatches, and phase transitions. The probability of forming a dense and protective Al_2O_3 scale increases with increasing aluminum activity at the surface. This can be done either by increasing the aluminum content in the intermetallic phase or by applying another chemical mechanism such as the fluorine effect. In the case of aluminized tantalum, the intermetallic phase with the highest aluminum content in the binary phase diagram is already formed during pack cementation. However, the growth rate of Ta_2O_5 and its volume increase during oxidation are too high and cannot be impeded by Al_2O_3 formation. Evolved stresses are released by crack formation which depletes the aluminum reservoir by Al_2O_3 formation without forming a close scale. Additionally, after pack cementation the intermetallic Al_3Ta phase already shows intergranular cracks providing oxygen diffusion paths into the sample, again increasing the probability of porous Ta_2O_5 formation. Hence, the selectivity of aluminum oxidation must be increased at the aluminized substrate surface and at the crack surfaces in the intermetallic phase. This is done using the halogen effect: The aluminum activity is increased and a closed Al_2O_3 layer forms (see Fig. 8a). Similar to TiAl alloys, the positive effect of the fluorine treatment is limited to a certain surface coverage window (see oxidation experiments for 40 h). Above this window halogen corrosion takes place, whereas below this, fluorine content is not present in sufficient amount to promote a closed scale formation. It was found that aluminized

tantalum substrates with an increased amount of fluorine treatment per surface used on TiAl alloys show oxidation resistance up to 100 h at 1300 °C in synthetic air (see Fig. 11b). To analyze the oxide growth kinetics, the TGA curve is fitted with the general oxidation Eq. 1 where $\frac{\Delta m}{A}$ is the weight change per surface area, n an exponent, and k is the oxidation constant (for $n = \frac{1}{2}$ it is called parabolic oxidation constant) [21].

$$\frac{\Delta m}{A} = (k \cdot t)^n \tag{1}$$

The fit is added to Fig. 11b. The micrographs confirm that oxidation protection is achieved due to the formation of a protective and closed Al_2O_3 scale (see Fig. 12b). With a thickness of around 5.9 ± 0.6 μm (see Table 3) this layer is also rather thin, which is a sign of low aluminum depletion of the intermetallic phase during Al_2O_3 formation. Hence, a low amount of stress and thus cracks had formed during oxide growth even with the intermetallic phase changes from Al_3Ta to $Al_{69}Ta_{39}$ [22]. Depletion of the aluminum reservoir is also high due to inward diffusion of aluminum into the tantalum substrate. In between the $Al_{69}Ta_{39}$ phase and the tantalum substrate, a second (AlTa) and third ($AlTa_2$) intermetallic phase formed and the total interdiffusion layer thickness increased more than five times compared to the just pack-aluminized sample. Furthermore, Kirkendall porosity is found caused by the aluminum diffusion processes. In contrast to the other refractory metals, fluorine was still detected after oxidation in the intermetallic layers and in the substrate material, so the selectivity of aluminum oxidation is still supported during further oxidation.

For tantalum, the fitting parameters of Eq. 1 are listed in Table 4. The oxidation of tantalum shows subparabolic behavior as was also described by Quadakkers et al. for Fe–Cr–Al-alloys [21]. Quadakkers showed near-cubic behavior due to the increase of the oxide's grain size during oxidation time. However, in this case n is even lower than 0.33 because the oxidation mechanism is different. Rapid initial growth takes place due to fast growing tantalum-rich oxides. In addition, in the case of a fluorine-treated sample, volatile aluminum fluorides form which are subsequently oxidized and form the Al_2O_3 scale. Diffusion of gaseous species is faster than in solid solution, hence, the alumina scale grows faster than without a fluorine treatment. After closure of the Al_2O_3 scale, the oxide growth slows down.

Table 4 Fitting parameters of Eq. 1 for mass change curves of the 100 h experiments at 1300 °C in synthetic air

	Ta + Al + 2× F	Nb + Al + F	W + Al + F
k [$\frac{g^n}{cm^{2n} \cdot s}$]	0.0061 ± 0.0001	0.0466 ± 0.0002	0.0028 ± 0.0001
n	0.257 ± 0.004	0.324 ± 0.003	0.213 ± 0.004

Oxidation of Niobium

For the same reasons as in the case of uncoated tantalum, uncoated niobium shows linear mass gain characteristics as well (see Fig. 5b). Aluminizing of niobium by pack cementation slows down its oxidation rate, and the onset of degenerative linear oxidation is retarded. However, similar to uncoated niobium, the whole substrate material is oxidized after 12 h at 1300 °C in synthetic air. The oxide growth rate of the aluminized sample is determined by linear fits in both regions. Up to 6 h it is around 2.8 mg/cm^{2}h and afterwards it changes to 83.4 mg/cm^{2}h. The delay is achieved due to the formation of a non-protective Al_2O_3 scale on Al_3Nb as described by Svedberg et al. and Steinhorst et al. [23, 24] for oxidation experiments on Al_3Nb substrates at a temperature of 1200 °C in air. They observed oxygen permeable Al_2O_3 scales with $NbAlO_4$ below, leading to spallation.

Applying PTFE to aluminized niobium greatly increases the oxidation resistance of the sample. In the 100-h oxidation test, the onset of accelerated oxide growth is shifted from 6 h to around 46 h. Up to this point, the oxidation kinetics seems to be parabolic and can be fitted using Eq. 1 as shown in Fig. 11a. The fitting parameters are again listed in Table 4. No closed protective oxide layers form after 100 h of oxidation as shown in Fig. 12a, because after 46 h, linear mass gain occurred.

The reason for alumina scale destruction and therefore its non-protective effect is explained in the following. During oxidation the surface is depleted in aluminum and a phase change of Al_3Nb to $AlNb_2$ occurs as shown in the micrographs. However, phases with lower aluminum content than the originally formed intermetallic phase are not only observed at the interface substrate/intermetallic phase but also at the interface oxide scale/intermetallic phase (see EPMA element maps in Fig. 9). This indicates high aluminum depletion through oxide scale formation, which also becomes obvious by looking at the oxide scale thicknesses given in Table 2. Compared to the other refractory metals, 2–3 times thicker oxide scales are found on niobium. This suggests a high concentration of flaws in the oxide layer system. Looking at the coating experiments, it is found that after pack aluminizing niobium shows the highest amount of cracks in the intermetallic phase. These cracks serve as diffusion paths of oxygen into the sample promoting the oxidation of niobium preferentially at the intermetallic/bulk material interface. Nb_2O_5 forms, which is linked with a high volume increase leading to spallation of the intermetallic aluminum reservoir. Besides stresses induced during the coating process, stresses caused by phase transformations, lattice mismatches and layer growth lead to further crack formation in intermetallic phases and in the protective oxide layer. In areas with high crack formation, the aluminum reservoir is already fully consumed after 12h and the substrate is locally oxidized (see Fig. 8c). After 100 h no protective oxide layer or intermetallic phase is left and the whole surface is covered with Nb_2O_5. The change in TGA slope marks the break away after depletion of the aluminum reservoir. After the break away, the growth of Nb_5O_3 oxide can no longer be slowed down. Svedberg et al. showed that $NbAl_2$ does not resist oxidation [23]. However, on the aluminized and fluorine-treated sample, an Al_2O_3 layer is even formed on $AlNb_2$. This shows the positive effect of halogen

treatment in increasing the aluminum activity in AlNb$_2$ and making the selective formation of Al$_2$O$_3$ possible. Hence in the case of aluminized and fluorine-treated niobium not only Al$_3$Nb but also AlNb$_2$ is an alumina former. This effect also retards the onset of the fast oxidation from 6h for the just aluminized sample on which the AlNb$_2$ shows no oxidation resistance to 46h for the aluminized and additionally fluorine-treated sample.

However, even fluorine additions could not provide oxidation resistance for 100 h at 1300 °C. To overcome this problem, the origin of induced stresses has to be clarified in the future and possible concepts to reduce the stresses—such as using an AlNb$_2$ and PTFE coating instead of Al$_3$Nb and PTFE—should be investigated.

Oxidation of Molybdenum

In contrast to other refractory metals, uncoated molybdenum shows a mass loss characteristic (see Fig. 5d). This behavior is expected for oxidation of molybdenum at 1300 °C in dry air, because MoO$_3$ is the most stable oxide at high oxygen partial pressures and is volatile above 800 °C. Hence, protective layer systems are needed suppressing the evaporation of the substrate material.

Comparing the aluminized molybdenum substrates with and without fluorine treatment, both show comparable mass change curves and cross sections with similar layers and layer thicknesses (see Figs. 5d, 7 and the molybdenum substrates in Table 2). In contrast to the other refractory metals, the halogen effect is not needed on aluminized molybdenum to enhance selective aluminum oxidation. The difference between molybdenum and the other substrate materials is its different oxide growth mechanism. Molybdenum forms volatile oxides while all other metals principally form fast growing oxides at 1300 °C. Thus, on aluminized molybdenum no voluminous fast growing oxides can hinder the closing of the Al$_2$O$_3$ scale as observed with niobium and tungsten. The formation of volatile oxides even enhances the alumina scale formation in the beginning of the oxidation process because the molybdenum atoms at the surface are evaporated while aluminum remains.

The 100-h TGA measurement (see Fig. 11d) shows not only a mass increase but also a mass loss. It can be fitted using Eq. 2 [25] which includes a loss term along with the parabolic mass increase. The equation describes the so-called paralinear growth. The best fitting parameter for the parabolic rate constant K_P is 0.0265 ± 0.0001 g^2/cm^4s and for the linear weight loss rate A it is 0.084 ± 0.004 g/cm^2s. The fit is added to Fig. 5d.

$$\frac{\Delta m}{A} = (K_P \cdot t)^{0.5} - A \cdot t \qquad (2)$$

In order to investigate the process during oxidation, first the micrographs after 12 h of oxidation are analyzed (see Fig. 7a, c). The intermetallic phase Al$_8$Mo$_3$ at the sample surface is depleted of aluminum which reacts with oxygen to form the protective Al$_2$O$_3$ scale. This causes the formation of AlMo$_3$ underneath the oxide scale. Simultaneously, aluminum diffuses into the bulk material which leads to

additional depletion of the aluminum reservoir. An $AlMo_3$ interdiffusion layer is also formed in between Al_8Mo_3 and the molybdenum substrate. Both depletion effects seem to be comparable on samples with and without additional halogen treatment. After 100 h, the area underneath Al_2O_3 is further depleted and metallic molybdenum is formed locally which becomes obvious by examination of the BSE image in Fig. 13b. In addition, in the areas of complete consumption of Al_8Mo_3 phase, cracks in the Al_2O_3 scale are found (see Fig. 13a). The formed Al_2O_3 scale is thick compared to the results obtained on tantalum (see Table 3), which indicates again, a high amount of cracks in the protective scale. As already mentioned, stresses are always induced into coating scales during oxide growth; however, their magnitude depends on lattice parameter mismatches, oxidation-caused volume increases, and phase transitions. In the case of molybdenum, the monoclinic Al_8Mo_3 transforms into cubic $AlMo_3$ during oxidation which probably induces high stresses inducing numerous cracks and thereby high aluminum depletion of the surface. Stress peaks mostly occur locally. In local failure sites, more aluminum is consumed to close the cracks. Due to the fact that aluminum diffusion in $AlMo_3$ is not fast enough to provide enough aluminum at the crack surfaces, the areas deplete even further and metallic molybdenum is left locally. In the case of further crack formation, oxygen can now react with metallic molybdenum. Volatile MoO_3 forms which spalls off the scale, further destroying the protective effect of the alumina layer. Increasing the oxidation time increases the aluminum reservoir depletion and therefore the formation of volatile MoO_3. A mass loss occurs.

To summarize, the challenge with molybdenum and at the same time its advantage is the volatility of its oxides which means that no additional fluorine treatment is required in order to increase the aluminum activity. However, a concept increasing the lifetime of aluminized molybdenum could be the formation of another intermetallic aluminum reservoir layer such as $AlMo_3$. This phase has a cubic crystal structure which could make it a better match for the cubic crystal structure of the substrate material, inducing less stress during depletion.

Oxidation of Tungsten

At 1300 °C, tungsten has two stable oxides, WO_2 and WO_3. Above 1300 °C, the sublimation of WO_3 starts [26], but the mass change curve in Fig. 5c reveals predominantly linear oxide growth characteristics. Obviously, oxide evaporation plays a minor role. Aluminizing of tungsten causes no significant increase in oxidation resistance. Again, an additional fluorine treatment after aluminizing greatly decreases the rate of oxide growth. In the 100-h oxidation experiments, aluminized and fluorine-treated tungsten also shows subparabolic growth kinetics which can be fitted by Eq. 1 (see Fig. 11c). The attempt of fitting with an additional mass loss term confirms that oxide evaporation can be neglected. The reasons for the subparabolic growth kinetic in this case are the fast growing tungsten oxides forming in the initial oxidation stage. However, no closed and protective Al_2O_3 layer is formed, neither after 12 h nor after 100 h of oxidation (see Figs. 8e, 12c). The oxidation seems to be suppressed by the presence of the Al_4W phase hindering oxygen diffusion to the tungsten substrate. Aluminum in the Al_4W phase is not

Table 5 Pilling–Bedworth ratio of relevant oxides after [29]

Oxide	Al_2O_3	Ta_2O_5	Nb_2O_5	MoO_3	WO_3
P–B ratio	1.29	2.44	2.68	3.25	3.38
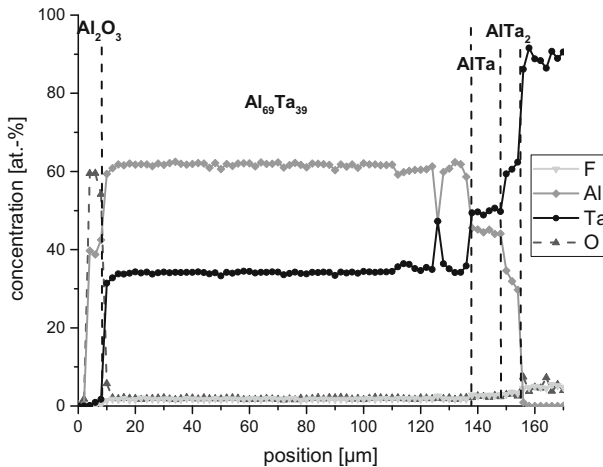
Fig. 14 Concentration profiles of aluminum, tantalum, oxygen, and fluorine in the subsurface zone of the aluminized and fluorine-treated tantalum substrate after 100 h of oxidation in synthetic air. The line scan was measured from the surface (position 0 μm) perpendicular into the sample

selectively oxidized to form a protective alumina layer, but Al_4W particles spall off. These particles are covered with Al_2O_3 (see Fig. 8e), preventing the oxidation of the Al_4W phase. The reason for the aluminum reservoir spallation seems to be the low increase in selectivity of aluminum oxidation and the high P–B ratio of tungsten (see Table 5) which is around 30 % higher compared to Nb_2O_5 and Ta_2O_5. Al_4W is a very brittle phase due to its high aluminum content and its monoclinic crystal structure. This supports crack propagation through the whole intermetallic layer which was already observed after pack cementation (see Fig. 4c). Oxygen diffuses through cracks and reacts with tungsten. The high volume increase during oxidation appears increasingly at the Al_4W/substrate interface, which spalls off the intermetallic phase or induces more cracks, leading to stronger oxygen attack. Due to the fact that no other intermetallic phase with lower aluminum contents exists in the binary Al–W system, no intermetallic phase can form in between Al_4W and the tungsten substrate by interdiffusion. Hence, no second phase can hinder crack propagation at the substrate interface due to a change in lattice structure or serve as bond coat. Therefore, oxygen can directly attack the substrate material by diffusing through the cracks in the intermetallic phase (Fig. 14).

For future research, silicon diffusion layers would be more promising for tungsten because no monoclinic intermetallic phases form and more intermetallic

phases with varying tungsten contents exist in the binary Si–W phase diagram. It is also important to mention that the formation of WO_3 is very critical in the presence of Al_2O_3 because they form eutectic phases with melting points below 1230 °C [27] which could even affect the integrity of the furnace components. This side effect could be also avoided by using silicon diffusion coatings.

Summary and Conclusion

Aluminum diffusion coatings have been applied successfully on the four different refractory metals niobium, tantalum, tungsten, and molybdenum. After a pack cementation process for 8 h at 1000 °C, smooth and homogeneous diffusion layers consisting of intermetallic phases with high aluminum contents were identified. Compared to experiments in the literature, the formation of predicted phases were confirmed in the cases of niobium and tungsten and the identified main intermetallic phase formed on molybdenum is in good agreement with the prediction made in the beginning of this work based on thermodynamic calculations.

During oxidation tests at 1300 °C in dry air, it was found that aluminizing has no effect on the oxidation resistance of tantalum and tungsten. In contrast, aluminizing niobium retards the linear oxide growth typically observed with niobium. A high increase in oxidation resistance is achieved using a halogen treatment on aluminized samples. Compared to our own experiments and experiments reported in the literature, the halogen effect has greatly improved the oxidation resistance of the refractory metals. Aluminized and fluorine-treated tantalum shows oxidation resistance up to 100 h at 1300 °C in dry air. A protective Al_2O_3 layer forms and a fluorine-containing aluminum reservoir below the alumina scale is maintained. It was found that the surface coverage ratio of fluorine plays a critical role especially for tantalum. In contrast, fluorine has no enhancing effect on molybdenum. The volatile MoO_3 oxides themselves promote the increase of aluminum activity at the surface resulting in the formation of Al_2O_3. The disadvantage of the oxide's volatility is that protective layer systems on molybdenum are prone to local failures and no closed and therefore protective alumina scales could be established on molybdenum substrates with an Al_8Mo_3 intermetallic surface layer. Aluminum diffusion coatings on tungsten serving as oxidation protection are very hard to produce due to the lack of different intermetallic phases with higher tungsten contents. In all cases, a critical factor for aluminum diffusion coatings is induced stresses due to the lattice parameter mismatch between substrate and intermetallic phases. Additional stresses induced through phase transformations due to aluminum depletion should be minimized by carefully selecting the intermetallic phases.

Looking at the morphology of the pack-aluminized samples, it is found that cracks generated in the intermetallic phase during the pack cementation process disturb the formation of a protective scale. The reason for the induced stress in the refractory metal aluminide phases is the mismatch of thermal expansion coefficient or lattice parameters between the bulk material and the intermetallic phases. In the worst case, the stresses do not only create intergranular cracks but also intragranular cracks, as observed with niobium, which has a strong effect on its oxidation

kinetics. One way of reducing stresses is the formation of another intermetallic phase with, for instance, a lower aluminum content. Another possibility lies in the thickness reduction of the intermetallic phase since in thicker layers induced stresses are more likely to become critical [28]. However, decreasing the layer thickness or the intermetallic phase's aluminum content directly decreases the aluminum reservoir at the sample surface, which decreases the oxidation performance. Hence, the pack parameters have to be chosen very carefully in order to balance a high aluminum reservoir with low-induced stresses.

To sum up, closed and protective Al_2O_3 layers were found on aluminized and fluorine-treated tantalum which therefore seems to be very promising. Total lifetime investigations should be carried out in the future after optimization of the fluorine treatment on tantalum. Aluminized molybdenum substrates also show promising mechanisms suitable to increase their oxidation resistance even without the need of an additional fluorine treatment. Reducing the induced stresses due to phase transformation of the intermetallic phase during aluminum depletion would be a promising approach to optimize protective aluminum diffusion coatings on molybdenum. We propose the formation of an $AlMo_3$ intermetallic phase via pack cementation instead of Al_8Mo_3. The feasibility of meeting critical issues, such as aluminum reservoir depletion by inward diffusion by further alloying of the surface area could also be investigated. One promising concept is the generation of phases with low aluminum solubility similar to T_2 phase on Mo–Si–B alloys [9]. Layers with low aluminum solubility hinder the aluminum diffusion in the surface area, and thereby reduce the aluminum reservoir depletion and increase the lifetime.

References

1. B. Bewlay, L. Cretegny, M. Jackson, and P. Subramanian, *JSPS Report of the 123rd Committee on Heat Resistant Materials and Alloys* **48**, 261 (2007).
2. P. Jéhanno, H. Kestler, A. Venskutonis, M. Böning, M. Heilmaier, B. Bewlay, and M. Jackson, *Metallurgical and Materials Transactions A* **36**, 515 (2005).
3. Z. Tang, A. J. Thom, M. Kramer, and M. Akinc, *Intermetallics* **16**, 1125 (2008).
4. K. Ito, T. Hayashi, M. Yokobayashi, and H. Numakura, *Intermetallics* **12**, 407 (2004).
5. K. Ito, T. Murakami, K. Adachi, and M. Yamaguchi, *Intermetallics* **11**, 763 (2003).
6. R. Sakidja, J. Park, J. Hamann, and J. Perepezko, *Scripta Materialia* **53**, 723 (2005).
7. S. Majumdar, I. Sharma, and A. Suri, *International Journal of Refractory Metals and Hard Materials* **26**, 549 (2008).
8. S. Chakraborty, S. Banerjee, I. Sharma, and A. Suri, *Journal of Nuclear Materials* **403**, 152 (2010).
9. R. Sakidja, F. Rioult, J. Werner, and J. Perepezko, *Scripta Materialia* **55**, 903 (2006).
10. S. Majumdar, A. Arya, I. Sharma, A. Suri, and S. Banerjee, *Applied Surface Science* **257**, 635 (2010).
11. S. Majumdar, P. Sengupta, G. B. Kale, and I. G. Sharma, *Surface and Coatings Technology* **200**, 3713 (2006).
12. A. Donchev, E. Richter, M. Schütze, and R. Yankov, *Intermetallics* **14**, 1168 (2006).
13. A. Donchev and M. Schütze, *Materials Science Forum*, Vol. 461 (Trans Tech Publications, Pfaffikon, 2004), pp. 447–454.

14. A. Naji, M. Galetz, and M. Schütze, *Materials and Corrosion* **66**, 863 (2015).
15. A. Donchev and M. Schütze, Patent (EP), 2008.
16. A. Naji, M. C. Galetz, and M. Schütze, *Materials and Corrosion* **65**, 312 (2014).
17. C. Bale, P. Chartrand, S. Degterov, G. Eriksson, K. Hack, R. B. Mahfoud, J. Melanççon, A. Pelton, and S. Petersen, *Calphad* **26**, 189 (2002).
18. J. Grüters and M. Galetz, *Intermetallics* **60**, 19 (2015).
19. S.Wöllmer, S. Zaefferer, M. Göken, T. Mack, and U. Glatzel, *Surface and Coatings Technology* **167**, 83 (2003).
20. A. Donchev, B. Gleeson, and M. Schütze, *Intermetallics* **11**, 387 (2003).
21. W. Quadakkers, D. Naumenko, E. Wessel, V. Kochubey, and L. Singheiser, *Oxidation of Metals* **61**, 17 (2004).
22. V. Witusiewicz, A. Bondar, U. Hecht, J. Zollinger, V. Petyukh, O. Fomichov, V. Voblikov, and S. Rex, *Intermetallics* **18**, 92 (2010).
23. R. Svedberg, Z. Foroulis, and F. Pettit, *Properties of High Temperature Alloys*. (The Electrochemical Society, Pennington, 1976), p. 331.
24. M. Steinhorst and H. Grabke, *Materials Science and Engineering A* **120**, 55 (1989).
25. A. Soleimani-Dorcheh, W. Donner, and M. C. Galetz, *Materials and Corrosion* **65**, 1143 (2014).
26. O. Lu-Steffes, R. Sakidja, J. Bero, and J. Perepezko, *Surface and Coatings Technology* **207**, 614 (2012).
27. I. L. Shabalin, *Ultra-High Temperature Materials I: Carbon (Graphene/Graphite) and Refractory Metals*, Vol. 1. (Springer, New York, 2014).
28. M. Nagl, W. Evans, S. Saunders, and D. Hall, *Materials Science and Technology* **8**, 1043 (1992).
29. E. McCafferty, *Introduction to Corrosion Science*. (Springer, New York, 2010).
30. R. Davies, A. Dinsdale, J. Gisby, J. Robinson, and S. Martin, *Calphad* **26**, 229 (2002).